Ecological Informatics 92 (2025) 103470

Contents lists available at ScienceDirect

Ecological Informatics

journal homepage: www.elsevier.com/locate/ecolinf

Consistent nutrient mapping from Sentinel-2 and Sentinel-3 in nearshore waters: A case study in Xiamen Bay

Wendian Lai [a], Xiaolong Yu [a,b,c,*], Nengwang Chen [c], Caiyun Zhang [a], Yufang Wu [d], Shuiying Huang [c], Lingling Li [a], Zhongping Lee [a,b]

[a] State Key Laboratory of Marine Environmental Science, College of Ocean and Earth Sciences, Xiamen University, Xiamen 361102, China
[b] Fujian Ocean Innovation Center, Xiamen 361102, China
[c] Fujian Provincial Key Laboratory for Coastal Ecology and Environmental Studies, College of the Environment and Ecology, Xiamen University, Xiamen 361102, China
[d] Xiamen Environmental Monitoring Station, Xiamen 361022, China

ARTICLE INFO

Keywords:
Nutrient remote sensing
High spatial resolution
Machine learning
Satellite data fusion
Sentinel-2
Optically complex waters

ABSTRACT

High-resolution monitoring of nutrient concentrations is essential for assessing water quality in coastal and bay regions. This study proposes a two-step framework to map dissolved inorganic nitrogen (DIN) and phosphorus (DIP) concentrations at high spatial resolution in Xiamen Bay (XMB). First, the nutrient retrieval models, termed AutoGluon-DIN/DIP, were trained using matchups between radiometric measurements from Sentinel-3 Ocean and Land Color Instrument (OLCI, 300 m resolution) and *in situ* nutrient observations. The high revisit frequency of OLCI enabled the compilation of a large and representative training dataset. Then, a cross-sensor transfer model, termed AutoGluon-transfer, was developed to convert Sentinel-2 Multi Spectral Instrument (MSI, resampled to 10 m) reflectance data into OLCI-equivalent bands, enabling the implementation of OLCI-trained models on MSI imagery. The key inputs of AutoGluon-DIN/DIP were the Rayleigh scattering-corrected top-of-atmosphere reflectance ($\rho_{rc}(\lambda)$) at eight bands common to both MSI and OLCI. Validation against *in situ* data showed that AutoGluon-DIN/DIP outperformed other machine learning models, with a root mean squared difference of 0.11 mg L^{-1} for DIN and 0.012 mg L^{-1} for DIP ($N = 636$). The retrieved DIN/DIP values also aligned well with independent buoy measurements in both magnitude and temporal variation (coefficient of determination $R^2 \sim 0.6$, $N = 382$). The AutoGluon-transfer effectively converts MSI-measured $\rho_{rc}(\lambda)$ to OLCI-equivalent bands ($R^2 > 0.8$), yielding nutrient maps that are consistent with those from OLCI in both magnitude and spatial pattern. Overall, the proposed framework offers a promising solution for high-resolution nutrient monitoring in coastal waters.

1. Introduction

Nutrients such as nitrogen and phosphorus are crucial for phytoplankton growth, which supports primary production and diverse biological networks (Chen et al., 2013a). However, excess nutrients, often resulting from anthropogenic activities such as agriculture, urban runoff, and industrial discharges, can lead to eutrophication. This process degrades water quality, disrupts ecological balance, and causes harmful algal blooms (HABs) (Anand et al., 2024; Davidson et al., 2014; Li et al., 2024a; Zheng et al., 2023), which threaten water resources, marine life, and local economies dependent on fisheries and tourism. Dissolved inorganic nitrogen (DIN) and dissolved inorganic phosphorus (DIP) are widely used to characterize nutrient levels and are deemed the key water quality parameters (WQPs) (Howarth et al., 2000; Li et al., 2024b).

Traditional water quality assessments rely on moored instruments, drifting buoys, and *in situ* sampling. While these methods provide accurate and reliable data, they offer limited spatial and temporal coverage, making it challenging to capture the dynamic and heterogeneous distribution of nutrients in coastal waters (Bierman et al., 2011). Remote sensing technology provides a promising alternative, enabling large-scale and frequent observations of marine environments. However, WQPs are not optically active and therefore cannot be directly detected by satellite (Sathyendranath et al., 1991). To address this,

* Corresponding author at: State Key Laboratory of Marine Environmental Science, College of Ocean and Earth Sciences, Xiamen University, Xiamen 361102, China.
E-mail address: xlyu@xmu.edu.cn (X. Yu).

https://doi.org/10.1016/j.ecoinf.2025.103470
Received 19 May 2025; Received in revised form 8 October 2025; Accepted 8 October 2025
Available online 14 October 2025

previous studies have explored empirical relationships between WQPs and satellite-derived environmental variables, such as sea surface temperature (SST) (Pan et al., 2018; Poornima et al., 2016; Sarangi, 2011), chlorophyll-a concentration (Chl) (Poornima et al., 2019; Silió-Calzada et al., 2008), and sea surface salinity (SSS) (Wang et al., 2018; Yu et al., 2021). While these variables can be retrieved from satellite data, they are affected by a complex interplay of biophysical factors, including physical mixing, upwelling, biological activity, and chemical reactions (Chen et al., 2023). In contrast, machine learning techniques offer a significant advantage in capturing complex, nonlinear relationships between remote sensing measurements and WQPs, without the need for explicit physical formulations.

Recent advances in machine learning have significantly improved the capability of remote sensing for WQPs retrievals. For instance, Unnithan et al. (2025) developed a dense deep learning model for aquatic remote sensing applications to estimate total suspended solids and dissolved organic carbon in coastal regions of southeastern Australia. Chen et al. (2024) applied a stacking random forest model to estimate DIN in the Northwest Pacific using MODIS-observed SST and Chl. Xia et al. (2024) found that the eXtreme Gradient Boosting (XGBoost) algorithm outperformed other commonly used machine learning models in estimating total nitrogen concentration in Poyang Lake, the largest freshwater lake in China. Similarly, Zhu et al. (2024) demonstrated that XGBoost was the most effective for retrieving DIN in the Northern South China Sea coastal waters when SST and Chl, SSS, sea surface current (SSC), and depth were used as inputs. He et al. (2025) proposed a novel quad-modality deep neural network that integrates R_{rs}, temporal features, and a custom environmental parameter to estimate Chl concentrations in Lianyungang's lakes, while Huang et al. (2023) used Sentinel-2 and Sentinel-3 R_{rs} with the Support Vector Machine (SVM) and Gaussian process regression (GPR) models to derive DIN and DIP in the offshore waters of Dayu Bay. It is noted that these previous studies predominantly focus on specific regions, utilizing mainly R_{rs}, R_{rs}-derivative products (Chl), SST, outputs from ocean models (SSS, SSC), and satellite metadata, including longitude, latitude, and date. However, R_{rs} and its derivatives are particularly sensitive to atmospheric correction algorithms, especially in coastal regions. Failure of atmospheric correction can result in missing or inaccurate R_{rs} data (Wang, 2002, 2005), thereby compromising the retrievals of WQPs. Moreover, monitoring nutrient dynamics in small-scale estuaries and bays requires high-spatial-resolution data for all variables involved in retrieval models, which remains a significant challenge (Huang et al., 2023). These limitations underscore the need for advanced, high-spatial-resolution remote sensing frameworks explicitly designed for complex coastal environments.

Xiamen Bay (XMB), located on the southeastern coast of China, is considered one of the most important bays in Fujian Province. Substantial nutrient inputs from the Jiulong River make XMB highly susceptible to eutrophication (Chen et al., 2013b). Rapid economic development has exacerbated eutrophication issues, leading to frequent and harmful algal blooms (He et al., 2022). Urban expansion and industrial activities have increased nutrient influx, heightening the risk of ecological degradation (Lu et al., 2023). Nutrient levels in Xiamen Bay (XMB) fluctuate seasonally due to river discharge, anthropogenic pollution (including sewage, animal waste, and agricultural runoff), and oceanic exchange processes. These dynamic influences create significant challenges for water quality management. Therefore, there is a pressing need for accurate and high-spatiotemporal monitoring approaches to support near-real-time assessment of nutrient levels in XMB.

In this study, we developed a novel framework to retrieve DIN and DIP in XMB at high spatiotemporal resolution by leveraging the frequent revisit capability of Sentinel-3 Ocean and Land Color Instrument (OLCI) and the high spatial resolution of Sentinel-2 Multi Spectral Instrument (MSI). Another key innovation is the use of Rayleigh scattering-corrected top-of-atmosphere reflectance ($\rho_{rc}(\lambda)$) as model input. This approach avoids the uncertainties associated with atmospheric correction in nearshore waters and significantly improves the accuracy of nutrient retrievals. The proposed framework comprises several machine learning models based on the AutoGluon: two models for DIN and DIP retrieval (AutoGluon-DIN/DIP) and eight for cross-sensor data fusion (AutoGluon-transfer). The fusion models convert $\rho_{rc}(\lambda)$ at eight MSI bands into the equivalent OLCI bands, enabling OLCI-trained nutrient models to be directly applied to MSI data and supporting consistent, high spatial resolution nutrient mapping in XMB. The data, methods, results, and discussion are detailed in the following sections.

2. Data and methods

2.1. The overall framework for high-spatial-resolution nutrients mapping

The high revisit frequency of OLCI enables more matchups with *in situ* measurements. Thus, we first developed nutrient retrieval models based on matched OLCI-measured $\rho_{rc}(\lambda)$ and *in situ* nutrients measurements. The developed models were then validated using independent datasets. However, due to the relatively coarse spatial resolution of OLCI, its applicability for fine-scale mapping is limited in coastal waters. To overcome this challenge, we proposed a cross-sensor fusion model that enables the implementation of OLCI-based nutrient retrieval models on MSI data, thereby generating high-resolution nutrient maps for the XMB. The technical workflow of this study is illustrated in Fig. 1, consisting of three main phases: data preprocessing, model development, and model validation and application.

In the data preprocessing phase (Fig. 1(a)), the *in situ*-measured DIN and DIP were matched with high revisit, low spatial resolution (300 m) OLCI observations on the same day (termed satellite-*in situ* matchups). These matchups were essential, as direct matchups between MSI and *in situ* data alone did not yield sufficient samples for effective model training. In addition, MSI and OLCI images acquired on the same day were also paired, forming a matchup dataset of MSI- and OLCI-measured $\rho_{rc}(\lambda)$ (termed cross-sensor matchups).

During the model development phase (Fig. 1(b)), OLCI-based AutoGluon-DIN/DIP models were trained using satellite-*in situ* matchups to derive DIN/DIP concentrations from OLCI-measured $\rho_{rc}(\lambda)$. In parallel, AutoGluon-transfer models were developed using the cross-sensor matchups to convert MSI-measured $\rho_{rc}(\lambda)$ into $\rho_{rc}(\lambda)$ at equivalent OLCI bands.

In the validation and application phase (Fig. 1(c)), the AutoGluon-DIN/DIP models were evaluated using both the developing and validation datasets. These models were then applied to OLCI images to generate time-series maps of DIN and DIP in XMB at 300 m spatial resolution. The high-resolution nutrient maps were finally obtained by sequentially applying the AutoGluon-transfer and AutoGluon-DIN/DIP models to MSI data.

2.2. In situ measurements

The *in situ* measurements of DIN and DIP were compiled from three sources, with the sampling locations shown in Fig. 2.

1) Monitoring data: The data were mainly collected in the XMB by the Xiamen City Environmental Monitoring Center Station (XCEMCS) between 2019 and 2022. To enhance the representativeness of the dataset, additional nutrient measurements from other coastal areas in Fujian Province outside of XMB were also incorporated. These data are publicly available and were obtained from the Department of Ecology and Environment of Fujian Province (DEEFP) (https://sthjt.fujian.gov.cn/). The sampling locations are shown as orange circles in Fig. 2(b).
2) Survey data: Field survey data were collected by research teams at Xiamen University from 2018 to 2022, with sampling locations represented by blue circles in Fig. 2(b). DIN and DIP concentrations in both the Monitoring and Survey data were measured using the

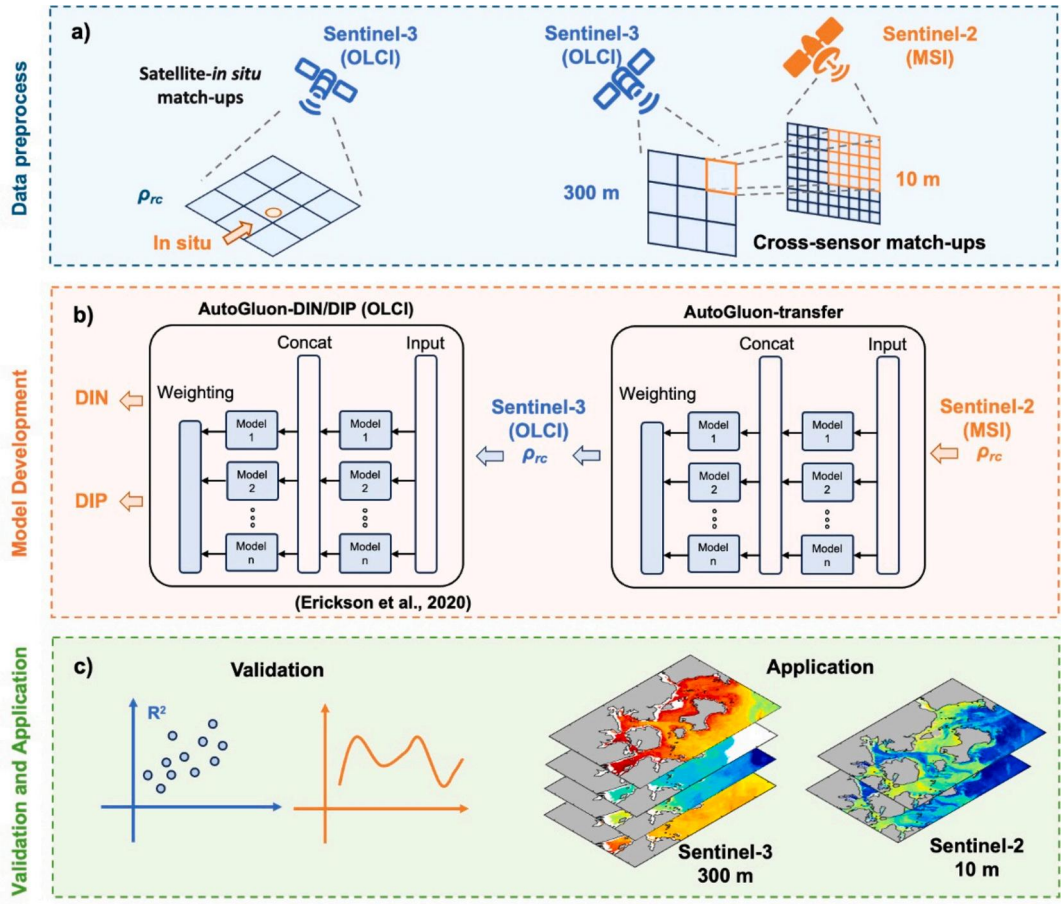

Fig. 1. The workflow for nutrient retrieval from Sentinel-3 and Sentinel-2.

same method, which involved water sampling, filtration, and laboratory analysis (Yu et al., 2020). Water samples were filtered on research vessels using GF/F (0.7 μm) Whatman glass microfiber filters, and the filtrates were stored in cool containers until laboratory analysis. In the laboratory, the filtrates were analyzed for NO_3-N, NO_2-N, NH_4-N, and $P_2O_5^-$ concentrations using a SEAL AutoAnalyzer 3. DIN was calculated as the sum of NO_3-N, NO_2-N, and NH_4-N, while DIP was measured as orthophosphate ($P_2O_5^-$). Instrument performance was verified using a standard reference material provided by the National Environmental Protection Agency for laboratory quality control, with deviations ranging from −1 % to +4 % from the standard concentrations.

3) Buoy data: High-frequency measurements were collected from four buoys positioned near the Huli Mountain (HLS, 118.10°E, 24.43°N), Yefengzhai (YFZ, 118.19°E, 24.45°N), Tong'an Bay (TAW, 118.17°E, 24.57°N), and Baozhu Island (BZY, 118.07°E, 24.54°N) between January and December 2022. The buoys' locations are represented by purple triangles in Fig. 2(c). DIN and DIP concentrations in the buoy data were automatically measured by the Nutrient Auto-Analyzer (Model is-3N1P, Hanhong Inc.) every 30 min. Note that the Nutrient Auto-Analyzer was calibrated monthly using laboratory measurements of DIN and DIP. Here, we employed only DIN and DIP buoy data within the 1st to 99th percentile range for the subsequent analysis to remove potential outliers from automatic measurements. The buoy data revealed that DIN and DIP concentrations from the four buoys exhibited similar seasonal patterns in 2022, with higher values from January to June (spring and summer) and lower values from July to December (autumn and winter).

2.3. Satellite data and processing

This study employed satellite measurements from the Sentinel-2 MSI and the Sentinel-3 OLCI for the nutrients mapping in XMB, where both data can be downloaded from the Copernicus Data Space Ecosystem (https://dataspace.copernicus.eu/explore-data). To ensure consistency in data processing and analysis across OLCI and MSI, we utilized the eight spectral bands common to both sensors in developing the AutoGluon-DIN/DIP and AutoGluon-transfer models. These bands have identical or closely matched center wavelengths. Table 1 outlines the spectral configuration and spatial resolution of these common bands in the visible to near-infrared (NIR) domain.

To circumvent atmospheric correction issues in the coastal regions, we used $\rho_{rc}(\lambda)$ for algorithm development in this study (Lai et al., 2022). The $\rho_{rc}(\lambda)$ is defined as

$$\rho_{rc}(\lambda) = \rho_t(\lambda) - \rho_r(\lambda) \quad (1)$$

where $\rho_t(\lambda)$ is the top-of-atmosphere reflectance, $\rho_r(\lambda)$ is the Rayleigh reflectance derived from a look-up table (LUT) generated by the 6SV model (Kotchenova et al., 2006; Vermote et al., 1997). The $\rho_t(\lambda)$ is defined as

$$\rho_t(\lambda) = \frac{\pi L_t(\lambda)}{t_g F_0(\lambda) cos(\theta_s)} \quad (2)$$

where $L_t(\lambda)$ is the sensor-measured radiance at the top-of-atmosphere, t_g is the gas transmittance, F_0 is the extraterrestrial solar irradiance, and θ_s is the solar zenith angle.

Level 1C products of MSI and OLCI were first downloaded and subsequently processed to $\rho_{rc}(\lambda)$ using the ACOLITE software (version

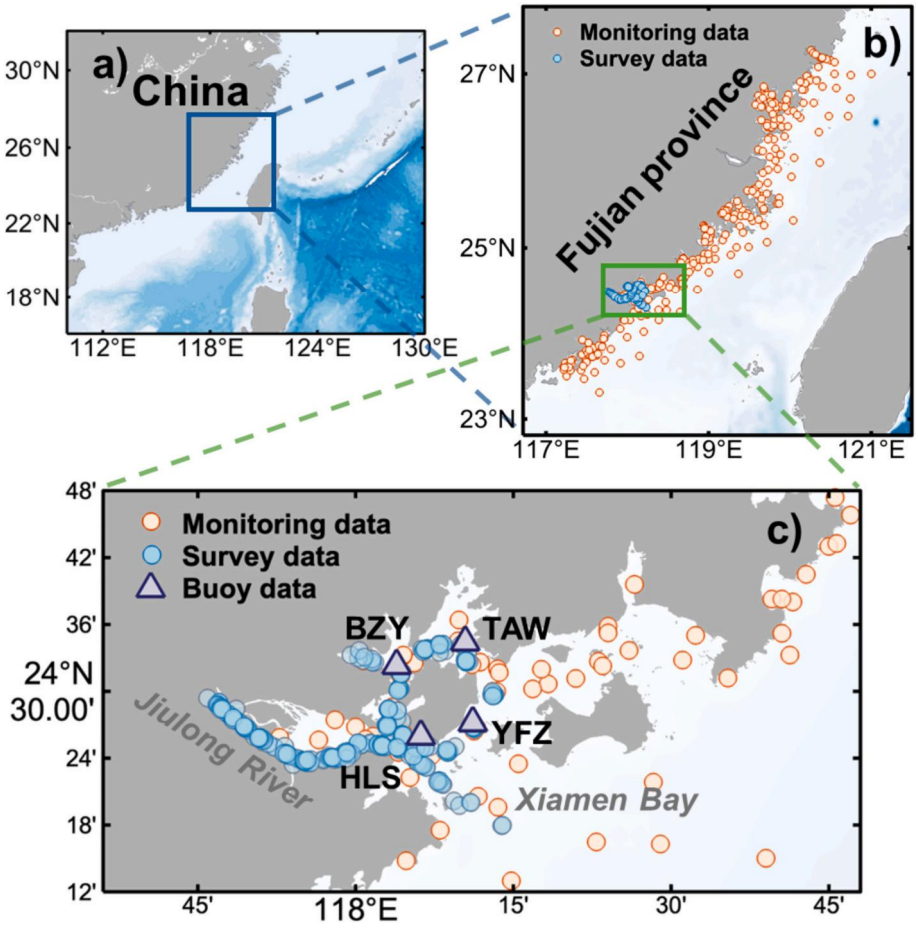

Fig. 2. Locations of *in situ* sampling and buoys.

Table 1
The spectral configuration and spatial resolution of the eight common bands between Sentinel-2 MSI and Sentinel-3 OLCI in the visible and near-infrared domain.

Sentinel-2 MSI			Sentinel-3 OLCI		
Band	Center wavelength (nm)	Spatial resolution (m)	Band	Center wavelength (nm)	Spatial resolution (m)
1	443	60	3	443	300
2	492	10	4	490	
3	560	10	6	560	
4	665	10	8	620	
5	704	20	11	709	
6	740	20	12	754	
7	783	20	16	779	
8a	865	20	17	865	

20231023.0, https://github.com/acolite/acolite/). ACOLITE automatically estimates $\rho_r(\lambda)$ and efficiently returns $\rho_{rc}(\lambda)$.

In this procedure, all MSI bands were resampled to a 10 m spatial resolution, while the OLCI bands were maintained at a 300 m spatial resolution. Since aerosol correction was not applied, cloud and land contamination pixels were manually excluded. Specifically, pixels with $\rho_{rc}(865) > 0.2$ were removed, as well as any pixel with $\rho_{rc}(\lambda) < 0$ or $\rho_{rc}(\lambda) > 1$ across all bands. Additionally, to minimize potential contamination from strong sun glint, pixels with $\rho_{rc}(1610) > 0.06$ were also masked out.

(1) Satellite-*in situ* matchups

The ρ_{rc} (λ) data from OLCI were matched with *in situ* observations, including the Monitoring data, Survey data, and Buoy data, using a 3 × 3 pixel window within the same day. A total of 692 OLCI images over XMB and other Fujian coastal regions (23°N–28°N, 117°E–122°E) from 2018 to 2023 were collected. Both Sentinel-3A and Sentinel-3B are equipped with OLCI. If an *in situ* nutrient measurement matched with both Sentinel-3A and Sentinel-3B, each was treated as an independent matchup. This strategy increased the number of valid matchups and reduced the model's dependency on the satellite platform. Each *in situ* nutrient measurement could be matched with up to 9 OLCI $\rho_{rc}(\lambda)$ spectra. Any spectrum with ρ_{rc} (620) deviating by more than 10 % from the 3 × 3 average was considered an outlier and excluded, as the 620 nm band is highly sensitive to turbidity and water dynamics in the study area. The remaining spectra were averaged to represent the satellite-measured $\rho_{rc}(\lambda)$ corresponding to each *in situ* data.

All the satellite-*in situ* matchups were categorized into two principal groups: the development and validation datasets (see Table 2 for details). The development dataset consists of matchups from the Monitoring data, Survey data, and three Buoys data (HLS, YFZ, and TAW). Within this dataset, 70 % of the data were randomly selected for model training (termed Nutrient-Train dataset), while the remaining 30 % were used for hyperparameter tuning (termed Nutrient-Tuning dataset). Model performance was evaluated on the Nutrient-Tuning dataset during training to facilitate manual hyperparameter adjustment and optimize overall model performance. The DIN and DIP measurements from the BZY buoy exhibited wide dynamic ranges and were selected as the independent validation dataset (see Table 2), which is hereafter termed the Nutrient-Val dataset.

(2) Cross-sensor matchups between OLCI and MSI

Table 2
Descriptions of the development and validation datasets used in this study. Min, Max, σ, and CV indicate the values of minimum, maximum, standard deviation, and coefficient of variation, respectively. N is the number of matchups.

Datasets	Source	Date	WQPs	Min	Max	Mean	σ	CV	N
				mg L^{-1}	mg L^{-1}	mg L^{-1}		(%)	
The development dataset (1. Nutrient-Train dataset, $N = 1481$; 2. Nutrient-Tuning dataset, $N = 636$)	Monitoring data	2018/01/01–2022/12/31	DIN	0.003	2.10	0.19	0.21	113.3	1027
			DIP	0.001	0.260	0.019	0.02	120.3	
	Survey data	2018/01/01–2022/12/31	DIN	0.05	1.27	0.61	0.32	51.9	74
			DIP	0.003	0.083	0.037	0.02	45.9	
	Buoy data (HLS, YFZ, and TAW)	2022/01/01–2022/12/31	DIN	0.11	1.24	0.43	0.23	52.8	1016
			DIP	0.006	0.069	0.034	0.02	46.4	
The validation dataset (Nutrient-Val dataset)	Buoy data (BZY)	2022/01/01–2022/12/31	DIN	0.15	1.07	0.47	0.19	39.2	390
			DIP	0.018	0.083	0.040	0.01	37.1	

To apply the OLCI-based nutrients model to high-spatial-resolution MSI images, transfer models were developed to convert MSI $\rho_{rc}(\lambda)$ data to OLCI-equivalent $\rho_{rc}(\lambda)$ data. For this purpose, we screened all MSI images over XMB in 2022 and matched them with OLCI images acquired on the same day, resulting in 44 image pairs spanning all seasons. Note that the difference between the acquisition time of paired MSI and OLCI images was mostly under one hour, during which water conditions can be assumed relatively stable. Here, we resampled MSI $\rho_{rc}(\lambda)$ data to align with the coordination of OLCI using the linear interpolation (MATLAB function *griddata*), yielding 363,190 pairs of $\rho_{rc}(\lambda)$ matchups. These matchups were then used as the development dataset for AutoGluon-transfer. Among them, 70 % (N = 254,233) were randomly selected for model training (termed the Transfer-Train dataset), and the remaining 30 % (N = 108,957) were used for model tuning (Transfer-Tuning dataset). In addition, an independent validation set (Transfer-Val dataset) was generated using the same-day OLCI and MSI measurements from Oct. 21, 2019, resulting in 48,293 matchups.

2.4. The machine learning models based on AutoGluon

A significant challenge in model development is the limited availability of training data. Automated Machine Learning addresses this issue by automating model selection and parameter optimization, reducing the need for manual tuning. AutoGluon, recognized for its efficiency and ease of use, streamlines these processes and facilitates the rapid deployment of high-performance machine learning models (Erickson et al., 2020). Its core strength lies in the sequential stacking of multiple models with minimal hyperparameter tuning (Fig. 1(b)). This multilayer stack ensemble integrates algorithms such as k-nearest neighbors, neural networks, LightGBM, random forests, Catboost, and XGBoost, and has been shown to outperform individual models (Van der Laan et al., 2007). To prevent overfitting, AutoGluon employs repeated k-fold bagging and Bayesian optimization during hyperparameter tuning (Caruana et al., 2025). Users can control the total training time, within which AutoGluon optimizes the ensemble, achieving high performance with minimal computational effort.

In this study, all the models were trained using Python 3.11 and AutoGluon version 1.0.0. During the model development phase (Fig. 1 (b)), we developed 10 AutoGluon models, where two of them are the AutoGluon-DIN/DIP model for DIN and DIP retrievals, and the remaining eight models are for converting MSI $\rho_{rc}(\lambda)$ to equivalent OLCI bands.

(a) OLCI-based AutoGluon-DIN/DIP models

The inputs for AutoGluon-DIN/DIP models include OLCI $\rho_{rc}(\lambda)$ at 443, 490, 560, 620, 709, 754, 779, and 865 nm, the ratio of $\rho_{rc}(\lambda$, except 560 nm) to $\rho_{rc}(560)$ (termed $\rho_{rc}(\lambda)^{\text{ratio}}$), and the acquisition date of the OLCI image. Our experiments demonstrated that incorporating the $\rho_{rc}(\lambda)^{\text{ratio}}$ could significantly enhance the model's performance during feature engineering. AutoGluon automatically extracts temporal features from the date variable, including year, month, day, and the day of the week. These features allow the model to capture seasonal cycles, weekly patterns, and other temporal patterns essential for accurate predictions of DIN and DIP. The model outputs are the logarithmic values of DIN and DIP, *i.e.,* ln(DIN) and *ln*(DIP), respectively. Using logarithmic values enhances the model's predictive accuracy and robustness by stabilizing the variance and reducing data skewness, thus ensuring that the developed models can be applied to a wide range of nutrient concentrations (Yasin et al., 2024). After extensive testing, we found that setting the stack levels to 1 and the bagging folds to 5 yields the highest nutrient retrieval accuracy in this study.

(b) AutoGluon-transfer models

Eight AutoGluon-transfer models were trained to convert MSI-measured $\rho_{rc}(\lambda)$ to OLCI-equivalent bands. Each model used the same inputs—$\rho_{rc}(\lambda)$ at eight MSI bands (443, 492, 560, 665, 704, 740, 783, and 865 nm)—and was designed to predict $\rho_{rc}(\lambda)$ at one specific OLCI band at 443, 490, 560, 620, 709, 754, 779, and 865 nm, respectively. These models were referred to as AutoGluon-transfer$_{443}$, AutoGluon-transfer$_{490}$, AutoGluon-transfer$_{560}$, AutoGluon-transfer$_{620}$, AutoGluon-transfer$_{709}$, AutoGluon-transfer$_{754}$, AutoGluon-transfer$_{779}$, and AutoGluon-transfer$_{865}$, respectively. All models were trained using the same configuration as the AutoGluon-DIN/DIP models, with the stack levels set to 1 and the bagging folds set to 5.

2.5. Accuracy assessment

We employed four metrics to evaluate the performance of the AutoGluon models, including the coefficient of determination (R^2), Root Mean Square Difference (RMSD), Median Absolute Relative Percentage Difference (MAPD), and Unbiased Relative Percentage Difference (URPD), and they are expressed as,

$$R^2 = 1 - \frac{\sum_{i=1}^{n}(y_i - \hat{y}_i)^2}{\sum_{i=1}^{n}(y_i - \overline{y})^2} \tag{3}$$

$$RMSD = \sqrt{\frac{1}{n}\sum_{i=1}^{n}(y_i - \hat{y}_i)^2} \tag{4}$$

$$MAPD = median\left\{\left|\frac{\hat{y}_i - y_i}{y_i}\right|\right\} \times 100\% \tag{5}$$

$$URPD = \frac{\hat{y}_i - y_i}{\hat{y}_i + y_i} \times 200\% \tag{6}$$

where y_i is the *in situ* value, $\overline{y}$ is the mean of the *in situ* value, $\hat{y}_i$ is the derived value from the model, and n is the total number of pairs used in

the analyses.

3. Results

3.1. Evaluation of AutoGluon-DIN/DIP models with in situ data

To assess the performance of the proposed AutoGluon-DIN/DIP models, the estimated DIN (DIN_{est}) was first validated against *in situ*-measured DIN ($DIN_{in\ situ}$) using the Nutrient-Train dataset. As shown in Fig. 3(a), the AutoGluon-DIN model demonstrated robust performance, with an R^2 of 0.86 and an RMSD of 0.10 mg L^{-1}. Notably, there were a few outliers in the predicted DIN, which could probably be attributed to the influence of cloud-contaminated or land-mixed pixels. Further validation was performed using the Nutrient-Tuning dataset (Fig. 3(b)). Similar to the results from the Nutrient-Train dataset, most data points were distributed around the 1:1 line, yielding an R^2 of 0.81 and RMSD of 0.11 mg L^{-1} for DIN ranging from 0.003 to 1.18 mg L^{-1}.

Fig. 3(c) and Fig. 3(d) display the relationship between the estimated DIP (DIP_{est}) and *in situ*-measured DIP ($DIP_{in\ situ}$) for the Nutrient-Train and Nutrient-Tuning datasets, respectively. The AutoGluon-DIP model achieved an R^2 of 0.83 and an RMSD of 0.01 mg L^{-1} on the Nutrient-Train dataset and an R^2 of 0.62 and an RMSD of 0.012 mg L^{-1} on the Nutrient-Tuning dataset, for DIP ranging from 0.001 to 0.14 mg L^{-1}. These results also demonstrate the robust performance of AutoGluon-DIP across different datasets.

To maximize the available training data, the AutoGluon-DIN/DIP models were retrained using the entire nutrient development dataset, combining both the Nutrient-Train and Nutrient-Tuning datasets. The retrained models were then used in subsequent analyses and applications. The final AutoGluon-DIN model achieved an R^2 of 0.88, an RMSD of 0.09 mg L^{-1}, and a MAPD of 11.5 %, while the final AutoGluon-DIP model achieved an R^2 of 0.80, an RMSD of 0.010 mg L^{-1}, and a MAPD of 9.6 %.

3.2. Independent validation of AutoGluon-DIN/DIP

The robustness and validity of the AutoGluon-DIN/DIP models were further evaluated using the Nutrient-Val dataset, which was not included in the model training. Fig. 4(a) and Fig. 4(b) illustrate the validation results for AutoGluon-DIN and AutoGluon-DIP, respectively. In Fig. 4(a), the grey line shows the daily average DIN from buoy measurements, with the light grey shading area indicating ±1 standard deviation (σ). The blue points represent DIN derived from the same day OLCI imagery, and the error bars reflect ±1 σ within the matched 3 × 3 pixels. A similar comparison is shown in Fig. 4(b) for DIP. Both models successfully capture the seasonal variation in nutrient levels, exhibiting higher concentrations from January to June and lower levels from July to December, which closely aligns with the original buoy data.

Statistical analysis further supports the consistency between model-estimated and *in situ*-measured DIN/DIP. The AutoGluon-DIN model achieved an R^2 of 0.55, an RMSD of 0.13 mg L^{-1}, and a MAPD of 21.6 %, indicating relatively low uncertainties compared to buoy measurements. Similarly, the AutoGluon-DIP model yielded an R^2 of 0.62, an RMSD of 0.013 mg L^{-1}, and a MAPD of 27.1 %. Despite the overall agreement, some discrepancies were observed. For example, the AutoGluon-DIP model systematically underestimated DIP in April and late September of 2022. These deviations may be due to quality issues in the buoy measurements or satellite imagery during those periods and require further investigation. Nevertheless, the overall good agreement between the model predictions and buoy observations supports the reliability of AutoGluon-DIN/DIP for monitoring nutrient concentrations in XMB.

3.3. Spatial-temporal distribution of DIN/DIP in XMB by OLCI

For each season, a representative cloud-free OLCI image was selected, and AutoGluon-DIN/DIP models were applied to retrieve the spatial distribution of DIN and DIP in XMB (Fig. 5 and Fig. 6). Overall, both nutrients exhibited similar spatial patterns throughout the year,

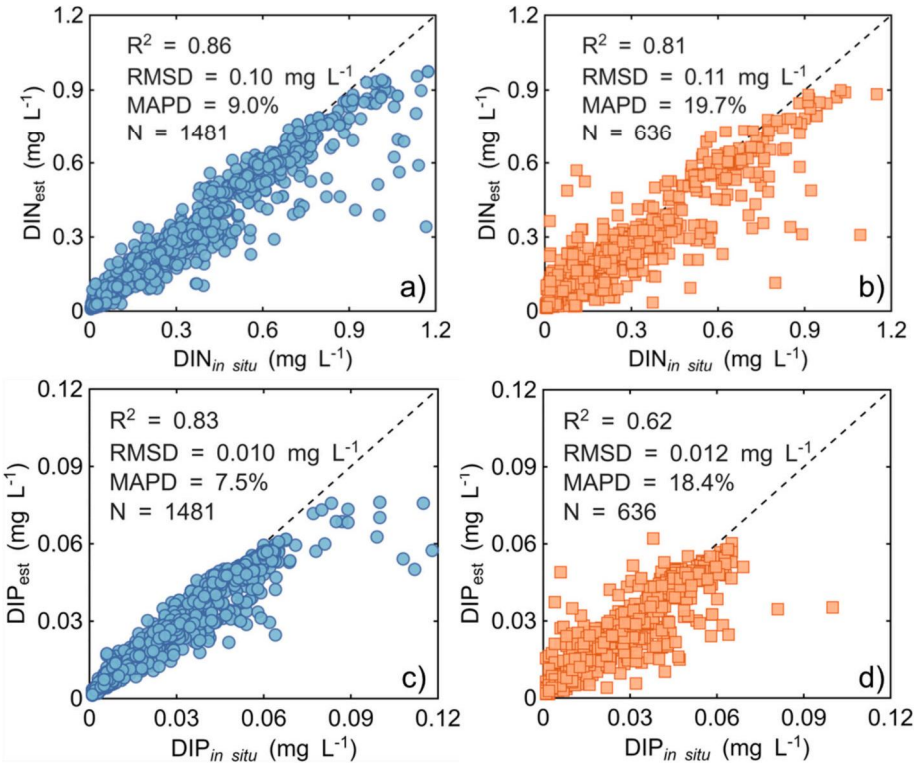

Fig. 3. The comparison of *in situ* measurements with AutoGluon-DIN/DIP estimations: (a) DIN in the Nutrient-Train dataset, (b) DIN in the Nutrient-Tuning dataset, (c) DIP in the Nutrient-Train dataset, and (d) DIP in the Nutrient-Tuning dataset.

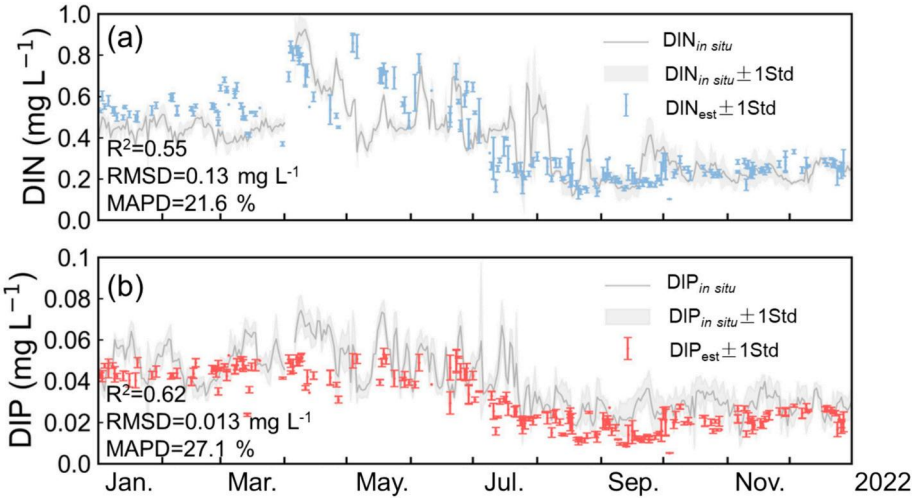

Fig. 4. The time series variation of AutoGluon-DIN/DIP estimated and *in situ* measured DIN (a) and DIP (b) from the Nutrient-Val dataset. The grey shaded area represents the daily average uncertainty of one standard deviation (σ). A gap in the data during early April is due to buoy measurement issues. The total number of DIN_{est} and DIP_{est} is 382.

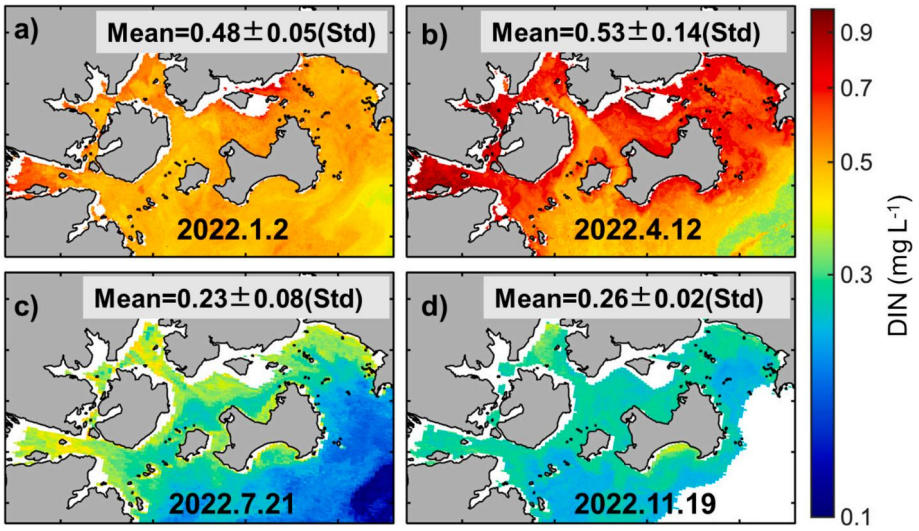

Fig. 5. AutoGluon-DIN model retrieved DIN distribution over XMB by OLCI images acquired in a) 2022.01.02; b) 2022.4.12; c) 2022.7.21; d) 2022.11.19. The mean and standard deviation for each image are shown in the grey box; the same applies to the figure below (units: mg L^{-1}).

with higher concentrations frequently observed in the inner bay areas (western and northern XMB), while lower levels were typically found in the open sea (Luo et al., 2022). Notably, the highest nutrient levels consistently occurred in estuarine zones, primarily due to substantial nutrient inputs from the discharge of the Jiulong River. Additionally, the distinct geomorphological and hydrodynamic characteristics of estuaries promote nutrient retention, thereby contributing to elevated nutrient concentrations in these areas (Ma et al., 2020).

Seasonal variation in DIN revealed a distinct peak in April (boreal spring), with a mean concentration of 0.53 mg L^{-1} in XMB, followed by January (boreal winter, 0.48 mg L^{-1}) and November (boreal autumn, 0.26 mg L^{-1}). The lowest nutrient level was observed in July (boreal summer), averaging at 0.23 mg L^{-1}. DIP exhibited a similar seasonal pattern, although its spring mean value (0.028 mg L^{-1}) was slightly lower than its winter mean (0.042 mg L^{-1}). This pattern aligns well with established expectations and is supported by buoy data (Fig. 4).

3.4. Evaluation of AutoGluon-transfer models

The MSI to OLCI $\rho_{rc}(\lambda)$ transfer models were evaluated with the Transfer-Tuning dataset (Fig. 7). Overall, the scatter points are closely distributed to the 1:1 line, indicating an exemplary mapping of MSI $\rho_{rc}(\lambda)$ to the OLCI bands using AutoGluon-transfer. The MAPDs for the MSI-converted $\rho_{rc}(\lambda)$ are generally below 5 % in the visible bands and under 10 % in the NIR bands. The elevated MAPD in the NIR is primarily due to the stronger atmospheric effects and low signal levels, which are dominated by aerosol contributions, making accurate prediction more challenging in nearshore waters (Wang, 2002, 2005).

Overall, the AutoGluon-transfer models offered a robust approach for capturing the complex relationships between $\rho_{rc}(\lambda)$ measurements at MSI and OLCI bands. Although AutoGluon-transfer exhibited comparatively lower performance in the NIR bands, this has a minimal impact on nutrient retrievals. As discussed in Sections 4.2 and 4.3, and Table 4, the models mainly rely on the "Image acquisition date" and the "$\rho_{rc}(490)^{ratio}$" as key predictors. As a result, deviations in the converted ρ_{rc}(NIR) do not significantly affect the accuracy of DIN/DIP retrievals.

3.5. High-spatial-resolution mapping of DIN/DIP from MSI

By utilizing AutoGluon-transfer, the AutoGluon-DIN/DIP models,

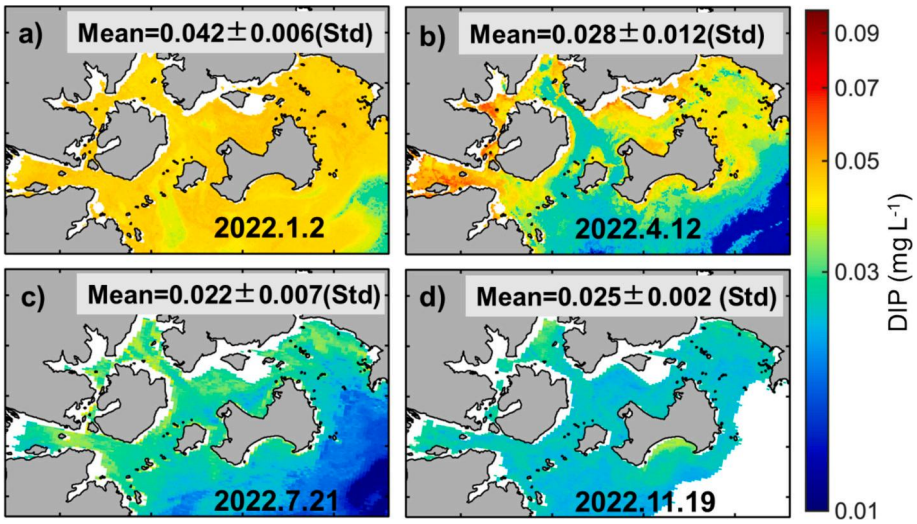

Fig. 6. Same as Fig. 5, but for derived DIP.

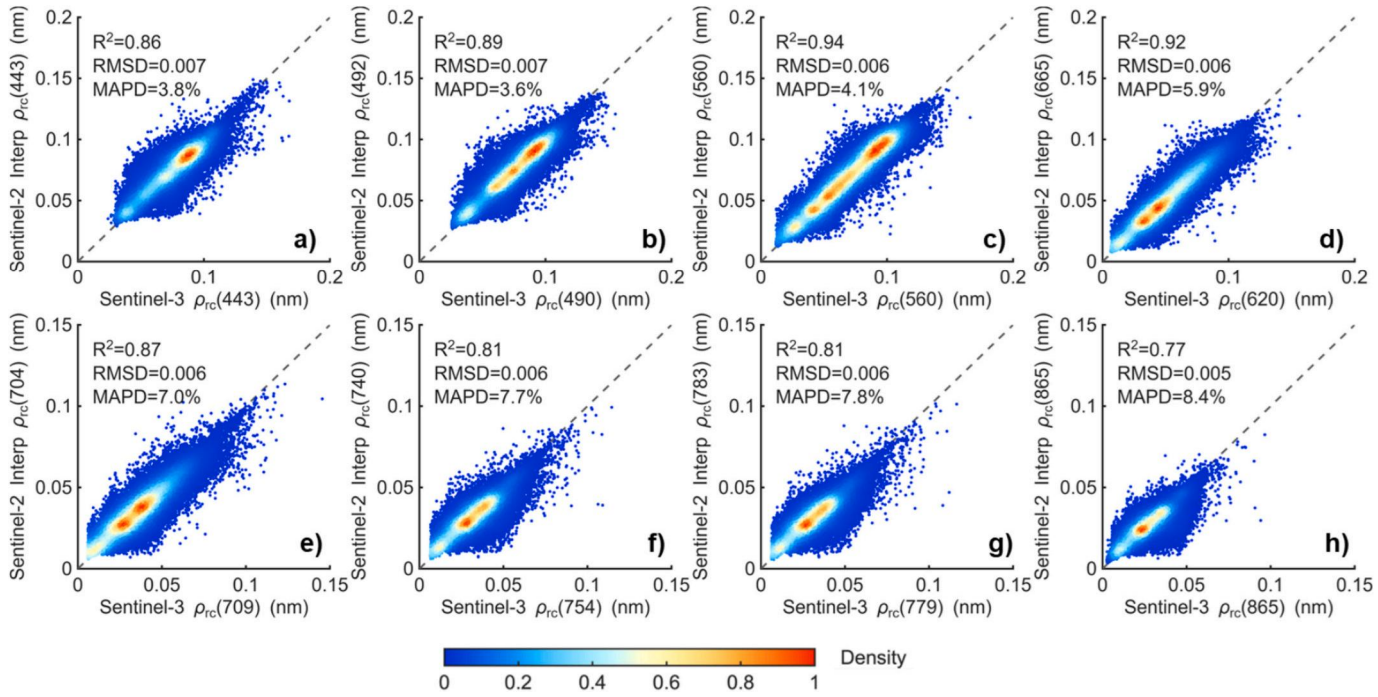

Fig. 7. The density scatter plots between OLCI-measured $\rho_{rc}(\lambda)$ and the MSI-converted $\rho_{rc}(\lambda)$ using AutoGluon-transfer for the Transfer-Tuning dataset (n = 108,957). The color bar represents the normalized density of samples, and the dotted line denotes the 1:1 line.

originally developed for OLCI data, can be applied to MSI $\rho_{rc}(\lambda)$ measurements, enabling the generation of high-spatial-resolution (10 m) nutrient maps in XMB. Fig. 8 presents the DIN and DIP distribution maps generated from MSI and OLCI imagery acquired on Oct. 21, 2019 (Transfer-Val dataset). The 10 m-resolution DIN and DIP maps derived from MSI are presented in Fig. 8(a) and Fig. 8(c), respectively, while their 300 m-resolution counterparts from OLCI are shown in Fig. 8(b) and Fig. 8(d). Notably, this MSI image was not included in the development of AutoGluon-transfer (see Section 2.3). Thus, the results shown in Fig. 8 serve as an independent evaluation of the effectiveness of combining AutoGluon-transfer with AutoGluon-DIN/DIP to generate nutrient maps from MSI data.

Overall, the spatial distribution patterns of DIN and DIP derived from MSI agree very well with those from OLCI (Fig. 8). This agreement is further confirmed by density scatter plots between MSI- and OCLI-derived nutrients, where most data points are closely aligned along the 1:1 line (Fig. 9). The R^2 values were 0.58 for DIN and 0.49 for DIP, with RMSDs of 0.06 mg L^{-1} and 0.005 mg L^{-1}, respectively. Note that MSI-derived DIN/DIP products (10 m spatial resolution) were first resampled to 300 m using linear interpolation to match OLCI measurements. Additionally, pixels with $\rho_{rc}(865)$ greater than 0.2 were masked to mitigate the impact of thin cloud contamination. Both MAPDs were below 20 %. These results are very promising for XMB, considering the wide dynamic range of DIN and DIP, and demonstrate that the proposed framework can effectively generate reasonable and high-spatial-resolution nutrient maps from MSI data in this region.

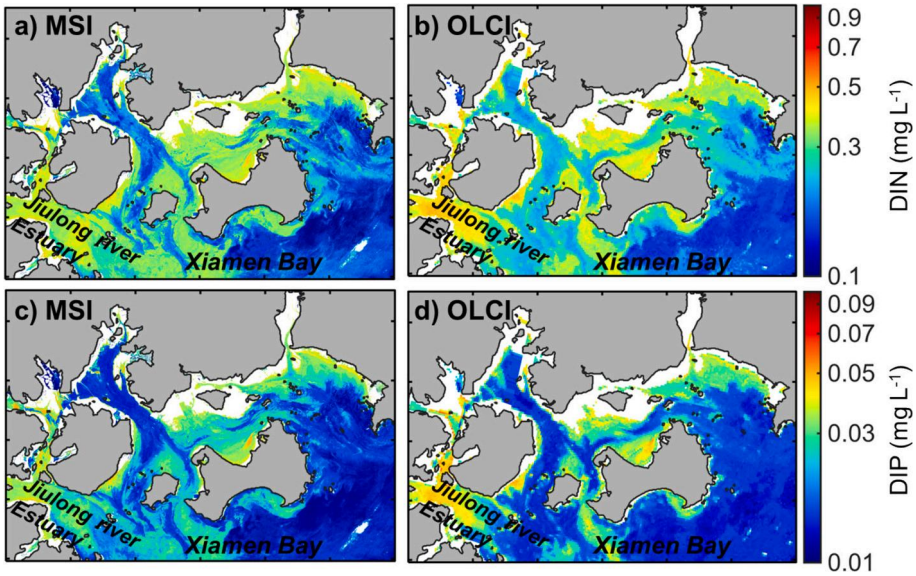

Fig. 8. The high-resolution (10 m) DIN (a) and DIP (c) distributions from the MSI image on Oct. 21, 2019, at 02:50:57 UTC, and the 300 m resolution DIN (b) and DIP (d) distributions from the OLCI image on Oct. 21, 2019, at 02:18:05 UTC.

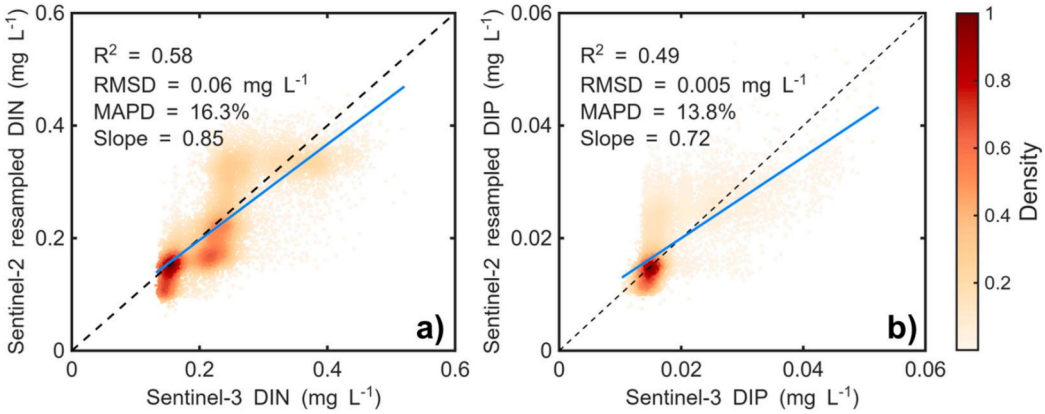

Fig. 9. The density scatter plot comparison between (a) OLCI DIN and MSI-resampled DIN and (b) OLCI DIP and MSI-resampled DIP (N = 12,539). The color bar represents the normalized density of samples, and the blue line represents the linear fit curve. (For interpretation of the references to color in this figure legend, the reader is referred to the web version of this article.)

4. Discussions

4.1. Model inter-comparisons

We evaluated the effectiveness of several widely used machine learning models for DIN prediction using the nutrient development dataset (Table 3). These models include AutoGluon (Erickson et al., 2020), Random Forest (Belgiu and Drăguţ, 2016), K-Nearest Neighbors (KNN) (Peterson, 2009), Gradient Boosting (Friedman, 2002), Decision Tree (Song and Ying, 2015), Support Vector Regression (SVR) (Smola and Schölkopf, 2004), and Multi-Layer Perceptron (MLP) (Rumelhart et al., 1986). To ensure a fair comparison, all models used the same input features as AutoGluon-DIN/DIP (see Section 2.4), with default parameter settings from the scikit-learn Python package. Since AutoGluon can automatically process the "image acquisition date" feature, we manually converted this variable into year, month, day, and day of the week as the inputs for the remaining models. In addition, all input variables were standardized using Z-score normalization to ensure that temporal features and $\rho_{rc}(\lambda)$ values were on a comparable scale.

Table 3
Performance of different machine learning models in predicting DIN using the Nutrient-Tuning dataset.

Model name	Nutrient-Tuning dataset		
	R^2	RMSD	MAPD (%)
AutoGluon	**0.81**	**0.11**	**19.7**
Random Forest	0.80	0.11	20.3
Decision Tree	0.66	0.15	22.2
Gradient Boosting	0.65	0.15	31.4
MLP	0.58	0.17	33.6
KNN	0.55	0.17	30.0
SVR	0.49	0.18	31.0

Table 3 summarizes the retrieval statistics for DIN across all models, with AutoGluon outperforming the others by achieving the highest R^2 of 0.81 and the lowest RMSD of 0.11 mg L^{-1}. For the remaining machine learning models, Random Forest performed relatively well, with an R^2 of 0.80 and an RMSD of 0.11 mg L^{-1}, followed by Decision Tree and Gradient Boosting. MLP, KNN, and SVR exhibited relatively larger uncertainties, with MLP showing a particularly high MAPD of 33.6 %.

The performance of machine learning models is heavily influenced by parameter tuning during the model development phase. The overall outstanding performance of AutoGluon could be attributed to its ability

to automatically optimize hyperparameters, enhance model stability, and improve generalization (Erickson et al., 2020). The performance of all these models in retrieving DIP was generally consistent with their results for DIN prediction (results not shown), further confirming that AutoGluon is the most effective approach for retrieving both DIN and DIP in this study.

4.2. Sensitivity analysis of the input features

To examine the influence of the input features on AutoGluon-DIN/DIP, we computed their feature importance scores (see Table 4), which were automatically generated by AutoGluon to highlight the relative contribution of each feature to model performance. Thus, these scores provide valuable insights into the key factors that drive the model outcomes. The importance scores were computed using permutation importance, which measures the drop in model accuracy when a specific feature is randomly shuffled (Altmann et al., 2010). A higher score indicates a stronger influence on the prediction, whereas a negative score suggests that removing the feature may improve model performance. As shown in Table 4, all features had positive importance scores, indicating that each input variable contributed constructively to the model's predictive accuracy.

The "Image acquisition date" is the most influential, underscoring the model's sensitivity to temporal changes and seasonal patterns. Several factors likely contribute to these: In boreal spring, cooler temperatures combined with increased rainfall in XMB lead to reduced marine biological activity and a substantial influx of terrestrial runoff into coastal waters, resulting in elevated DIN and DIP levels (Ma et al., 2020). During the dry season in boreal autumn, decreased rainfall shifts the primary nutrient sources to domestic sewage and industrial wastewater. These sources, typically characterized by high turbidity and significant amounts of dissolved organic matter and suspended solids, contribute to higher nutrient levels (Liu et al., 2021). In contrast, warmer SST and increased sunlight in summer drive rapid phytoplankton growth, which in turn depletes the available nutrients, leading to the lowest DIN and DIP levels of the year.

Followed by the "Image acquisition date", the second most important feature is the $\rho_{rc}(490)^{ratio}$. In general, light at 490 nm penetrates more deeply into the water column, and the reflectance at 490 nm could carry more information about in-water constituents among all bands. Moreover, the $\rho_{rc}(\lambda)^{ratio}$ emphasizes the spectral shape rather than the absolute magnitudes, which could also be closely related to the water constituents. This enables the model to more accurately capture the optical responses of water constituents to light, thereby enhancing both retrieval accuracy and model stability. Therefore, we recommend that future nutrient models prioritize incorporating these two parameters to improve retrieval accuracy.

Table 4
The feature importance scores of the AutoGluon-DIN/DIP model.

AutoGluon-DIN		AutoGluon-DIP	
Feature	Importance scores	Feature	Importance scores
Image acquisition date	0.94	Image acquisition date	0.73
$\rho_{rc}(490)^{ratio}$	0.28	$\rho_{rc}(490)^{ratio}$	0.19
$\rho_{rc}(754)^{ratio}$	0.09	$\rho_{rc}(665)^{ratio}$	0.09
$\rho_{rc}(443)^{ratio}$	0.07	$\rho_{rc}(754)^{ratio}$	0.08
$\rho_{rc}(665)^{ratio}$	0.07	$\rho_{rc}(665)^{ratio}$	0.08
$\rho_{rc}(709)^{ratio}$	0.06	$\rho_{rc}(443)^{ratio}$	0.07
$\rho_{rc}(665)^{ratio}$	0.06	$\rho_{rc}(709)^{ratio}$	0.07
$\rho_{rc}(779)^{ratio}$	0.05	$\rho_{rc}(779)^{ratio}$	0.06
$\rho_{rc}(865)^{ratio}$	0.05	$\rho_{rc}(754)$	0.05
$\rho_{rc}(490)$	0.05	$\rho_{rc}(865)^{ratio}$	0.05
$\rho_{rc}(560)$	0.04	$\rho_{rc}(560)$	0.05
$\rho_{rc}(754)$	0.04	$\rho_{rc}(443)$	0.04
$\rho_{rc}(443)$	0.04	$\rho_{rc}(490)$	0.04
$\rho_{rc}(709)$	0.03	$\rho_{rc}(779)$	0.03
$\rho_{rc}(865)$	0.03	$\rho_{rc}(709)$	0.03
$\rho_{rc}(779)$	0.02	$\rho_{rc}(865)$	0.02

4.3. Ablation study: quantifying the influence of input features on model performance

To further quantify the contribution of each input feature to the model's performance, we conducted an ablation study. Specifically, we removed one input variable group at a time and retained the model, such as date and $\varphi(\lambda)$, which was defined as a group of $\rho_{rc}(\lambda)$ and $\rho_{rc}(\lambda)^{ratio}$. For each modified input set, the model was retrained on the Nutrient-Train dataset and evaluated on the Nutrient-Tuning dataset. The variations in the error metrics, such as R^2, RMSD, and MAPD, were used to evaluate the relative importance of each input feature, with results summarized in Table 5 and Table 6 for DIN and DIP retrievals, respectively.

The ablation study reveals that including all features yields the best model performance. Notably, the image acquisition date contributes significantly to model accuracy. Removing this feature resulted in the most significant degradation for both models, with the R^2 and RMSD on the Nutrient-Tuning dataset dropping from 0.81 to 0.49 for DIN and from 0.62 to 0.39 for DIP. Correspondingly, MAPD increased markedly from 19.7 % to 37.8 % for DIN and from 18.4 % to 31.5 %. These results further confirm the critical role of temporal information in nutrient retrievals, as discussed in Section 4.2.

In contrast, removing each $\varphi(\lambda)$ had a much smaller impact, especially for the NIR bands. For instance, excluding φ(865), φ(779), φ(754), and φ(709) results in a decrease of 0.02 in R^2 and almost no change in MAPD. This is because ρ_{rc} values in the NIR are generally lower than those in the visible bands, and primarily represent aerosol signals, with little to no contribution from water constituent signal. Although their influence is limited, the NIR bands can still provide useful atmospheric information to the model, thereby indirectly helping to improve retrieval accuracy.

In addition, although removing certain features, such as φ(490), slightly improved the DIN model's performance, it generally reduced the accuracy of the DIP model, suggesting that the gain in DIN may be due to overfitting. As discussed in Section 4.2, the $\rho_{rc}(490)^{ratio}$ is an important predictor. In the perturbation-based approach described in Section 4.2, this feature is retained but perturbed with random noise, which reduces its individual contribution while preserving its correlations and joint

Table 5
Ablation study evaluating the influence of input features on DIN model performance.

Input features removed	Nutrient-Train dataset			Nutrient-Tuning dataset		
	R^2	RMSD	MAPD (%)	R^2	RMSD	MAPD (%)
None	0.86	0.10	9.0	0.81	0.11	19.7
Image acquisition date	0.85	0.13	18.4	0.49	0.19	37.8
φ(865)	0.86	0.11	10.9	0.81	0.11	18.3
φ(779)	0.86	0.11	11.1	0.80	0.12	18.8
φ(754)	0.88	0.10	9.5	0.81	0.11	17.7
φ(709)	0.85	0.11	10.0	0.80	0.11	18.2
φ(665)	0.86	0.11	10.4	0.80	0.11	18.2
$\rho_{rc}(560)$	0.87	0.10	10.1	0.81	0.11	18.3
φ(490)	0.89	0.10	9.9	0.81	0.11	18.8
φ(443)	0.85	0.11	10.7	0.80	0.12	19.1
φ(865), φ(779)	0.83	0.11	11.3	0.80	0.12	18.4
φ(865), φ(779), φ(754)	0.84	0.11	11.4	0.80	0.12	19.0
φ(865), φ(779), φ(754), φ(709)	0.86	0.11	10.7	0.81	0.11	19.1

Note: For convenience, we define a feature group $\varphi(\lambda)$ at wavelength λ as: $\varphi(\lambda) = \{\rho_{rc}(\lambda), \rho_{rc}(\lambda)^{ratio}\}$.

Table 6
DIP Ablation study evaluating the influence of input features on DIP model performance.

Input features removed	Nutrient-Train dataset			Nutrient-Tuning dataset		
	R^2	RMSD	MAPD (%)	R^2	RMSD	MAPD (%)
None	0.83	0.010	7.5	0.62	0.012	18.4
Image acquisition date	0.80	0.012	16.2	0.39	0.015	31.5
φ(865)	0.82	0.010	8.3	0.62	0.012	17.2
φ(779)	0.84	0.010	8.0	0.62	0.012	17.5
φ(754)	0.81	0.010	8.6	0.62	0.012	18.3
φ(709)	0.81	0.010	9.3	0.62	0.012	18.4
φ(665)	0.80	0.011	8.4	0.61	0.012	17.5
ρ_{rc}(560)	0.83	0.010	8.7	0.61	0.012	18.0
φ(490)	0.80	0.011	10.0	0.62	0.012	19.6
φ(443)	0.82	0.010	9.5	0.62	0.012	18.6
φ(865), φ(779)	0.80	0.010	8.6	0.63	0.012	18.1
φ(865), φ(779), φ(754)	0.82	0.010	8.9	0.62	0.012	19.4
φ(865), φ(779), φ(754), φ(709)	0.76	0.011	10.2	0.61	0.012	20.0

effects with other features. In contrast, the ablation study removes the feature entirely, disrupting these synergistic relationships. This disruption is particularly evident for the DIP model (Table 6), where removing φ(490) increased the MAPD from 18.4 % to 19.6 % in the Nutrient-Tuning dataset. This sensitivity suggests that DIP predictions depend more heavily on the combined information provided by φ(490) and other spectral features, and that eliminating it weakens the model's ability to capture these interdependencies. Therefore, using the full set of input features is considered the optimal strategy to balance model accuracy and generalization capability.

4.4. Advantages of using $\rho_{rc}(\lambda)$ as model inputs

Different from the conventional approach, we use $\rho_{rc}(\lambda)$ instead of $R_{rs}(\lambda)$ as model inputs, as using $R_{rs}(\lambda)$ as input could have several limitations. First, the amount of available training data is significantly reduced because many $R_{rs}(\lambda)$ values are invalid due to atmospheric correction failures (see Section 2.3) (Wang, 2002, 2005). Second, in optically complex coastal waters such as XMB, $R_{rs}(\lambda)$ products are often unreliable due to imperfect atmospheric correction, which introduces large uncertainties into subsequent retrievals of water-quality parameters (Wang et al., 2022). Lastly, when applying the model to satellite images, the number of valid pixels is substantially reduced, thus limiting the interpretation of the spatial-temporal variations of nutrients (Lai et al., 2022).

Mechanistically, when $\rho_{rc}(\lambda)$ is used as inputs, the AutoGluon model inherently incorporates the atmospheric correction process, allowing it to implicitly capture atmospheric effects through data-driven learning. This approach relies on a large and diverse dataset to effectively capture the variability of atmospheric conditions. More importantly, the atmospheric parameters that introduce the greatest uncertainties primarily affect the NIR spectral domains (Lai et al., 2022), which are not among the dominant features in the AutoGluon-DIN/DIP models. Therefore, using $\rho_{rc}(\lambda)$ as the model input could be more suitable for this study.

4.5. Uncertainty analysis of AutoGluon-DIN/DIP models

The uncertainties of AutoGluon-DIN/DIP models could stem from several factors. First, the nutrient development dataset is heavily concentrated in the low concentration range, leading to insufficient training on high nutrient values. Therefore, the retrieved nutrient values are less accurate at high values than at low ones. As a result, high nutrient concentrations tend to be underestimated (Fig. 3), despite the use of a logarithmic transformation of DIN and DIP during the training to stabilize the variance and reduce data skewness.

Second, the temporal window for the satellite and *in situ* matchups strongly affects the number of usable samples for model training. A narrow window reduces temporal mismatches but also substantially limits the amount of training data, which can hinder the development of a robust retrieval model. In this study, the window was set to within the same day to balance sample size and temporal consistency (Warren et al., 2019; Zhu et al., 2024), although notable changes in water conditions may still occur within a single day, particularly those caused by tidal variations.

4.6. Uncertainty analysis of cross-sensor data fusion

To assess the uncertainty and discrepancy between nutrient maps derived from the two sensors, we calculated the spatial distribution of the URPD between MSI- and OLCI-derived DIN products, as well as for DIP (Fig. 10), based on the retrieval results shown in Fig. 8. Note that DIN and DIP products from MSI were also resampled to OLCI resolution using linear interpolation, prior to the calculation of URPD. As highlighted by high URPD values, regions with relatively large discrepancies between OLCI and MSI measurements are primarily encountered in nearshore areas and the estuarine-ocean convergence zone. Several factors may contribute to the observed discrepancies. First, the high spatial heterogeneity of nutrients in these regions leads to differences between resampled MSI and OLCI data. Second, coastal water pixels are affected by the land adjacent effect. Third, errors in the MSI-converted $\rho_{rc}(\lambda)$ could be propagated to the estimated DIN/DIP products, contributing to the discrepancies in the nutrient maps between OLCI and MSI.

Additionally, tidal differences at the time of the two image acquisitions could lead to significant inconsistencies. For example, significant discrepancies in DIN and DIP are evident between the two sensors at the junction of the Jiulong River and XMB (southwest on the map, Fig. 10), as indicated by high URPD values. Although the two images were captured less than an hour apart, the tide level dropped from −1.8 m at the time of the OLCI overpass to −2.0 m during the MSI overpass. The tidal influence on nutrient concentration could be substantial, especially during low tide or ebb tide when water masses are more dynamic (Wisha and Maslukah, 2017), as was the case when both images were taken. Lower tides typically correspond to higher nutrient concentrations in coastal regions due to increased runoff contributions (Chen et al., 2013a). Consequently, the MSI-derived nutrient levels, captured during a lower tide, were higher than those observed in the OLCI products.

4.7. Limitations and perspectives

Many studies have shown that SST and SSS can exhibit linear or nonlinear relationships with DIN and DIP, playing a crucial role in nutrient retrieval, particularly in coastal waters (Arteaga et al., 2015; Pan et al., 2018; Silió-Calzada et al., 2008; Wang et al., 2018). However, the acquisition of reliable and high-spatial-resolution SST and SSS products in nearshore and small bay areas remains challenging, particularly for SSS (Klemas, 2011). For instance, the widely used SST product from MODIS has a spatial resolution of 1 km but is often contaminated by cloud cover. Satellite-derived SSS products from passive microwave radiometers, such as SMOS and SMAP, typically have coarser spatial resolutions (25–100 km) and are highly susceptible to land-sea contamination and radio frequency interference, leading to invalid observations in coastal zones (Kim et al., 2023).

Although some studies have shown that the potential of estimating SST and SSS using higher spatial resolution ocean color satellite, these products have not yet been operationally generated and are therefore not readily available (Chen and Hu, 2017; Kim et al., 2023; Xie et al., 2024). Thus, further research efforts are required to develop robust algorithms capable of providing high spatial-temporal resolution SSS and SST products before these variables can be effectively integrated into

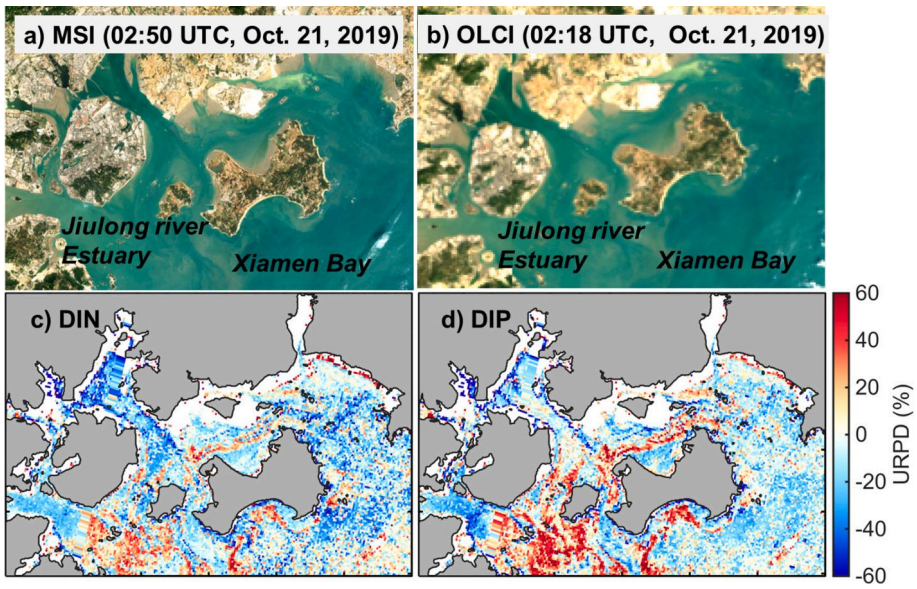

Fig. 10. RGB images of MSI on Oct. 21, 2019, at 02:50:57 UTC (a) and OLCI on Oct. 21, 2019, at 02:18:05 UTC (b), and the spatial distribution of Unbiased Relative Percentage Difference (URPD) between (c) MSI DIN (retrieved by AutoGluon-DIN and AutoGluon-transfer) and OLCI DIN (retrieved by AutoGluon-DIN) and (d) MSI DIP (retrieved by AutoGluon-DIN and AutoGluon-transfer) and OLCI DIP (retrieved by AutoGluon-DIP).

nutrient retrieval models. Such advancements are expected to substantially improve the accuracy and applicability of nutrient retrieval. Additionally, the framework proposed in this study is adaptable for retrieving SSS and SST when supported by a sufficiently large training dataset, offering a potential approach for water quality monitoring in estuaries and bays.

Another important limitation of this study is that the development dataset primarily consists of samples from XMB and the coastal waters of Fujian, which may limit the model's applicability and generalization to other regions with different optical and biogeochemical conditions. Expanding the development dataset to better represent diverse water conditions is crucial for improving the performance and generalizability of machine learning or neural network-based algorithms. Future work will focus on expanding the dataset by incorporating globally distributed open-access data sources and conducting field surveys across varied coastal environments.

5. Conclusions

This study proposed a novel framework based on AutoGluon to achieve high spatiotemporal resolution monitoring of DIN and DIP in XMB, by leveraging the high revisit frequency of OLCI and the high spatial resolution of MSI. First, DIN/DIP retrieval models (AutoGluon-DIN/DIP) were developed using OLCI-measured $\rho_{rc}(\lambda)$, ensuring a large number of satellite-*in situ* matchups for model training. Validation results demonstrated high accuracy of AutoGluon-DIN/DIP, with RMSDs of 0.11 mg L^{-1} for retrieved DIN and 0.012 mg L^{-1} for DIP, and R^2 around 0.6 when compared with independent buoy measurements. Second, we developed cross-sensor data fusion models (AutoGluon-transfer) to convert MSI-measured $\rho_{rc}(\lambda)$ into their OLCI equivalents. The MAPD for the MSI-converted $\rho_{rc}(\lambda)$ in the visible bands is generally less than 10 %. Independent validations demonstrate that the implementation of both AutoGluon-DIN/DIP and AutoGluon-transfer effectively generates high-spatial-resolution nutrient maps from MSI, yielding nutrient distribution patterns that are consistent and spatially coherent with those derived from OLCI.

Despite these promising results, several limitations remain: (1) some nutrient-related environmental variables, such as SST and SSS, were not included as model inputs due to limited data quality and spatial coverage in nearshore area; (2) the performance of AutoGluon-transfer in the NIR bands remains suboptimal, although these bands are not key predictors in AutoGluon-DIN/DIP; and (3) validation of the proposed framework in other nearshore regions may be necessary to strengthen confidence in its generalizability. Nevertheless, the proposed AutoGluon-based framework offers a promising and effective approach for high-resolution, consistent monitoring of DIN and DIP in optically complex coastal waters using data from multiple sensors, and can be readily adapted to monitor other water quality parameters.

CRediT authorship contribution statement

Wendian Lai: Writing – original draft, Visualization, Validation, Methodology. **Xiaolong Yu:** Writing – review & editing, Methodology, Funding acquisition, Conceptualization. **Nengwang Chen:** Writing – review & editing, Project administration. **Caiyun Zhang:** Writing – review & editing. **Yufang Wu:** Resources, Investigation. **Shuiying Huang:** Visualization. **Lingling Li:** Visualization. **Zhongping Lee:** Writing – review & editing, Supervision.

Declaration of competing interest

The authors declare that they have no known competing financial interests or personal relationships that could have appeared to influence the work reported in this paper.

Acknowledgements

This work was supported in part by the Guangxi Key R&D Program of China (contract No. GUIKE AB25069453), the National Science Foundation of China (42376173), the National Key Research and Development Program of China (2022YFC3105402), the Science and Technology Program of Xiamen, China (3502Z20226021), the Science and Technology Program of Fujian Province, China (2023Y4001), and the Fundamental Research Funds for the Central Universities. A portion of the data and samples were collected with support from the NSFC Shiptime Sharing Project (42249907, 42249904).

Data availability

Satellite measurements from the Sentinel-2 MSI and the Sentinel-3

OLCI are available from the Copernicus Data Space Ecosystem (https://dataspace.copernicus.eu/explore-data). The *in situ* measurements of DIN and DIP in XMB are under proprietary control but can be shared upon reasonable request. Additional *in situ* data from coastal areas of Fujian Province outside XMB were obtained from the Department of Ecology and Environment of Fujian Province and are publicly accessible at https://sthjt.fujian.gov.cn/. The source code for all models developed in this study is publicly available at https://github.com/wendian02/autogluon-nutrients.

References

Altmann, A., Toloşi, L., Sander, O., Lengauer, T., 2010. Permutation importance: a corrected feature importance measure. Bioinformatics 26, 1340–1347. https://doi.org/10.1093/bioinformatics/btq134.

Anand, V., Oinam, B., Wieprecht, S., 2024. Machine learning approach for water quality predictions based on multispectral satellite imageries. Eco. Inform. 84, 102868. https://doi.org/10.1016/j.ecoinf.2024.102868.

Arteaga, L., Pahlow, M., Oschlies, A., 2015. Global monthly sea surface nitrate fields estimated from remotely sensed sea surface temperature, chlorophyll, and modeled mixed layer depth. Geophys. Res. Lett. 42, 1130–1138. https://doi.org/10.1002/2014GL062937.

Belgiu, M., Drăguţ, L., 2016. Random forest in remote sensing: a review of applications and future directions. ISPRS J. Photogramm. Remote Sens. 114, 24–31. https://doi.org/10.1016/j.isprsjprs.2016.01.011.

Bierman, P., Lewis, M., Ostendorf, B., Tanner, J., 2011. A review of methods for analysing spatial and temporal patterns in coastal water quality. Ecol. Indic. 11, 103–114. https://doi.org/10.1016/j.ecolind.2009.11.001.

Caruana, R., Niculescu-Mizil, A., Crew, G., Ksikes, A., 2025. Ensemble selection from libraries of models. In: Proceedings of the Twenty-First International Conference on Machine learning, 18. https://doi.org/10.1145/1015330.1015432.

Chen, S., Hu, C., 2017. Estimating sea surface salinity in the northern Gulf of Mexico from satellite ocean color measurements. Remote Sens. Environ. 201, 115–132. https://doi.org/10.1016/j.rse.2017.09.004.

Chen, B., Ji, W., Chen, J., Lin, C., Huang, H., Huo, Y., Ji, X., 2013a. Characteristics of nutrients in the Jiulong River and its impact on Xiamen water, China. Chin. J. Oceanol. Limnol. 31, 1055–1063. https://doi.org/10.1007/s00343-013-2263-3.

Chen, N., Peng, B., Hong, H., Turyaheebwa, N., Cui, S., Mo, X., 2013b. Nutrient enrichment and N: P ratio decline in a coastal bay–river system in Southeast China: the need for a dual nutrient (N and P) management strategy. Ocean Coast. Manag. 81, 7–13. https://doi.org/10.1016/j.ocecoaman.2012.07.013.

Chen, S., Meng, Y., Lin, S., Yu, Y., Xi, J., 2023. Estimation of sea surface nitrate from space: current status and future potential. Sci. Total Environ. https://doi.org/10.1016/j.scitotenv.2023.165690, 165690.

Chen, S., Meng, Y., Shang, S., Zheng, M., Wang, Y., Chai, F., 2024. Remote estimates of sea surface nitrate and its trends from ocean color in the Northwest Pacific. J. Geophys. Res. Oceans 129, e2023JC019846. https://doi.org/10.1029/2023JC019846.

Davidson, K., Gowen, R.J., Harrison, P.J., Fleming, L.E., Hoagland, P., Moschonas, G., 2014. Anthropogenic nutrients and harmful algae in coastal waters. J. Environ. Manag. 146, 206–216. https://doi.org/10.1016/j.jenvman.2014.07.002.

Erickson, N., Mueller, J., Shirkov, A., Zhang, H., Larroy, P., Li, M., Smola, A., 2020. Autogluon-tabular: Robust and accurate automl for structured data. arXiv. https://doi.org/10.48550/arXiv.2003.06505 preprint arXiv:2003.06505.

Friedman, J.H., 2002. Stochastic gradient boosting. Comput. Stat. Data Anal. 38, 367–378. https://doi.org/10.1016/S0167-9473(01)00065-2.

He, X., Chen, C., Zhang, Z., Hu, H., Tan, A., Xing, Z., 2022. Temporal and spatial characteristics of harmful algal blooms in the offshore waters, China during 1990 to 2019. J. Appl. Remote. Sens. 16, 012004. https://doi.org/10.1117/1.JRS.16.012004.

He, H., Li, X., Wang, D., Qiao, W., Sun, Y., Han, Y., Zhang, F., Zhao, X., 2025. A novel quad-modality deep neural network for estimating chlorophyll-a concentrations in Lianyungang's lakes and reservoirs using sentinel-2 MSI data. Water Res. https://doi.org/10.1016/j.watres.2025.124246, 124246.

Howarth, R.W., Anderson, D., Cloern, J.E., Elfring, C., Hopkinson, C.S., Lapointe, B., Malone, T., Marcus, N., McGlathery, K., Sharpley, A.N., 2000. Nutrient pollution of coastal rivers, bays, and seas. Issues Ecol. 1–16.

Huang, J., Wang, D., Pan, S., Li, H., Gong, F., Hu, H., He, X., Bai, Y., Zheng, Z., 2023. A new high-resolution remote sensing monitoring method for nutrients in coastal waters. IEEE Trans. Geosci. Remote Sens. https://doi.org/10.1109/TGRS.2023.3294436.

Kim, Y.J., Han, D., Jang, E., Im, J., Sung, T., 2023. Remote sensing of sea surface salinity: challenges and research directions. GISci. Remote Sens. 60, 2166377. https://doi.org/10.1080/15481603.2023.2166377.

Klemas, V., 2011. Remote sensing of sea surface salinity: an overview with case studies. J. Coast. Res. 27, 830–838. https://doi.org/10.2112/JCOASTRES-D-11-00060.1.

Kotchenova, S.Y., Vermote, E.F., Matarrese, R., Klemm Jr., F.J., 2006. Validation of a vector version of the 6S radiative transfer code for atmospheric correction of satellite data. Part I: path radiance. Appl. Opt. 45, 6762–6774. https://doi.org/10.1364/AO.45.006762.

Lai, W., Lee, Z., Wang, J., Wang, Y., Garcia, R., Zhang, H., 2022. A portable algorithm to retrieve bottom depth of optically shallow waters from top-of-atmosphere measurements. J. Remote Sens. 2022. https://doi.org/10.34133/2022/9831947.

Li, H., Zhao, H., Wei, C., Cao, M., Zhang, J., Zhang, H., Yuan, D., 2024a. Assessing water quality environmental grades using hyperspectral images and a deep learning model: a case study in Jiangsu, China. Ecol. Inform. 84, 102854. https://doi.org/10.1016/j.ecoinf.2024.102854.

Li, J., Zheng, Z., Li, Y., Lyu, H., Ren, J., Cai, X., Du, C., Chen, N., Liu, G., Lei, S., 2024b. A hybrid algorithm for estimating total nitrogen from a large eutrophic plateau lake using Orbita hyperspectral (OHS) satellite imagery. Int. J. Appl. Earth Obs. Geoinf. 131, 103971. https://doi.org/10.1016/j.jag.2024.103971.

Liu, L., He, Q., Lan, J., Tian, Y., Zhang, J., Zhang, Y., Xu, W., 2021. Distribution characteristics of environmental factors and eutrophication assessment in the Fujian coastal areas. Mar. Sci. 45, 97–107. https://doi.org/10.11759/hykx20210105001.

Lu, X., Yu, W., Chen, B., Ma, Z., Chen, G., Ge, F., An, S., Han, W., 2023. Imbalanced phytoplankton C, N, P and its relationship with seawater nutrients in Xiamen Bay, China. Mar. Pollut. Bull. 187, 114566. https://doi.org/10.1016/j.marpolbul.2022.114566.

Luo, Y., Liu, J.-W., Wu, J.-W., Yuan, Z., Zhang, J.-W., Gao, C., Lin, Z.-Y., 2022. Comprehensive assessment of eutrophication in Xiamen Bay and its implications for management strategy in Southeast China. Int. J. Environ. Res. Public Health 19, 13055. https://doi.org/10.3390/ijerph192013055.

Ma, L., Lin, B.-L., Chen, C., Horiguchi, F., Eriguchi, T., Li, Y., Wang, X., 2020. A 3D-hydrodynamic model for predicting the environmental fate of chemical pollutants in Xiamen Bay, Southeast China. Environ. Pollut. 256, 113000. https://doi.org/10.1016/j.envpol.2019.113000.

Pan, X., Wong, G.T., Ho, T.-Y., Tai, J.-H., Liu, H., Liu, J., Shiah, F.-K., 2018. Remote sensing of surface [nitrite+ nitrate] in river-influenced shelf-seas: the northern South China Sea shelf-sea. Remote Sens. Environ. 210, 1–11. https://doi.org/10.1016/j.rse.2018.03.012.

Peterson, L.E., 2009. K-nearest neighbor. Scholarpedia 4, 1883. https://doi.org/10.4249/scholarpedia.1883.

Poornima, D., Shanthi, R., Ranith, R., Senthilnathan, L., Sarangi, R., Thangaradjou, T., Chauhan, P., 2016. Application of in-situ sensors (SUNA and thermal logger) in fine tuning the nitrate model of the bay of Bengal. Remote Sens. Appl. Soc. Environ. 4, 9–17. https://doi.org/10.1016/j.rsase.2016.04.002.

Poornima, D., Shanthi, R., Senthilnathan, L., Thangaradjou, T., Saravanakumar, A., Sarangi, R., 2019. decadal pattern of spatial and temporal variability of nitrate along the southwest bay of Bengal using remote sensing techniques. J. Indian Soc. Remote Sens. 47, 487–495. https://doi.org/10.1007/s12524-018-0915-7.

Rumelhart, D.E., Hinton, G.E., Williams, R.J., 1986. Learning representations by back-propagating errors. Nature 323, 533–536. https://doi.org/10.1038/323533a0.

Sarangi, R., 2011. Remote-sensing-based estimation of surface nitrate and its variability in the southern peninsular Indian waters. Int. J. Oceanogr. 2011. https://doi.org/10.1155/2011/172731.

Sathyendranath, S., Platt, T., Horne, E.P., Harrison, W.G., Ulloa, O., Outerbridge, R., Hoepffner, N., 1991. Estimation of new production in the ocean by compound remote sensing. Nature 353, 129–133. https://doi.org/10.1038/353129a0.

Silió-Calzada, A., Bricaud, A., Gentili, B., 2008. Estimates of sea surface nitrate concentrations from sea surface temperature and chlorophyll concentration in upwelling areas: a case study for the Benguela system. Remote Sens. Environ. 112, 3173–3180. https://doi.org/10.1016/j.rse.2008.03.014.

Smola, A.J., Schölkopf, B., 2004. A tutorial on support vector regression. Stat. Comput. 14, 199–222. https://doi.org/10.1023/B:STCO.0000035301.49549.88.

Song, Y.-Y., Ying, L., 2015. Decision tree methods: applications for classification and prediction. Shanghai Arch. Psychiatry 27, 130, 10.11919/j.issn.1002-0829.215044.

Unnithan, S.L.K., Cherukuru, N., Ingleton, T., Lehmann, E., Paget, M., Guo, Y., Drayson, N., Kerrisk, G., 2025. Mapping total suspended solids (TSS) and dissolved organic carbon (DOC) in complex coastal waters using deep learning enhanced remote sensing. Eco. Inform. 90, 103276. https://doi.org/10.1016/j.ecoinf.2025.103276.

Van der Laan, M.J., Polley, E.C., Hubbard, A.E., 2007. Super learner. Stat. Appl. Genet. Mol. Biol. 6. https://doi.org/10.2202/1544-6115.1309.

Vermote, E.F., Tanré, D., Deuze, J.L., Herman, M., Morcette, J.-J., 1997. Second simulation of the satellite signal in the solar spectrum, 6S: an overview. IEEE Trans. Geosci. Remote Sens. 35, 675–686. https://doi.org/10.1109/36.581987.

Wang, M., 2002. The Rayleigh lookup tables for the SeaWiFS data processing: accounting for the effects of ocean surface roughness. Int. J. Remote Sens. 23, 2693–2702. https://doi.org/10.1080/01431160110115591.

Wang, M., 2005. A refinement for the Rayleigh radiance computation with variation of the atmospheric pressure. Int. J. Remote Sens. 26, 5651–5663. https://doi.org/10.1080/01431160500168793.

Wang, D., Cui, Q., Gong, F., Wang, L., He, X., Bai, Y., 2018. Satellite retrieval of surface water nutrients in the coastal regions of the East China Sea. Remote Sens 10, 1896. https://doi.org/10.3390/rs10121896.

Wang, J., Wang, Y., Lee, Z., Wang, D., Chen, S., Lai, W., 2022. A revision of NASA SeaDAS atmospheric correction algorithm over turbid waters with artificial neural networks estimated remote-sensing reflectance in the near-infrared. ISPRS J. Photogramm. Remote Sens. 194, 235–249.

Warren, M.A., Simis, S.G., Martinez-Vicente, V., Poser, K., Bresciani, M., Alikas, K., Spyrakos, E., Giardino, C., Ansper, A., 2019. Assessment of atmospheric correction algorithms for the sentinel-2A MultiSpectral imager over coastal and inland waters. Remote Sens. Environ. 225, 267–289. https://doi.org/10.1016/j.rse.2019.03.018.

Wisha, U.J., Maslukah, L., 2017. Nutrient condition of Kampar big river estuary: distribution of N and P concentrations drifted by tidal bore" bono". Indones. J. Mar. Sci. 22. https://doi.org/10.14710/ik.ijms.22.3.137-146.

Xia, X., Pan, J., Pei, J., 2024. A new approach to estimate total nitrogen concentration in a seasonal lake based on multi-source data methodology. Eco. Inform. 83, 102807. https://doi.org/10.1016/j.ecoinf.2024.102807.

Xie, J., Lee, Z., Li, X., Wang, D., Zhang, C., Wu, Y., Yu, X., Zheng, Z., 2024. Estimation of sea surface temperature from Landsat-8 measurements via neural networks. IEEE J. Sel. Top. Appl. Earth Obs. Remote Sens. 17, 16306–16315. https://doi.org/10.1109/JSTARS.2024.3453908.

Yasin, M., Sarıgül, M., Avci, M., 2024. Logarithmic learning differential convolutional neural network. Neural Netw. 172, 106114. https://doi.org/10.1016/j.neunet.2024.106114.

Yu, D., Chen, N., Cheng, P., Yu, F., Hong, H., 2020. Hydrodynamic impacts on tidal-scale dissolved inorganic nitrogen cycling and export across the estuarine turbidity maxima to coast. Biogeochemistry 151, 81–98. https://doi.org/10.1007/s10533-020-00712-4.

Yu, X., Chen, S., Chai, F., 2021. Remote estimation of sea surface nitrate in the California current system from satellite ocean color measurements. IEEE Trans. Geosci. Remote Sens. 60, 1–17. https://doi.org/10.1109/TGRS.2021.3095099.

Zheng, Z., Huang, C., Li, Y., Lyu, H., Huang, C., Chen, N., Liu, G., Guo, Y., Lei, S., Zhang, R., 2023. A semi-analytical model to estimate chlorophyll-a spatial-temporal patterns from Orbita hyperspectral image in inland eutrophic waters. Sci. Total Environ. 904, 166785. https://doi.org/10.1016/j.scitotenv.2023.166785.

Zhu, L., Cui, T., Runa, A., Pan, X., Zhao, W., Xiang, J., Cao, M., 2024. Robust remote sensing retrieval of key eutrophication indicators in coastal waters based on explainable machine learning. ISPRS J. Photogramm. Remote Sens. 211, 262–280. https://doi.org/10.1016/j.isprsjprs.2024.04.007.